Achieving 19% efficiency in nonfused ring electron acceptor solar cells via solubility hysteresis sequential condensation strategy

Rui Zeng[1,10], Ming Zhang[1,10], Xiaodong Wang[2,10], Lei Zhu[1], Bonan Hao[1], Wenkai Zhong[1], Guanqing Zhou[1], Jiawei Deng[1], Senke Tan[1], Jiaxin Zhuang[1], Fei Han[1], Anyang Zhang[1], Zichun Zhou[1], Xiaonan Xue[4], Shengjie Xu[1], Jinqiu Xu[1], Yahui Liu[2], Hao Lu[2], Xuefei Wu[6], Cheng Wang[5], Zachary Fink[6,7], Thomas P. Russell[6,7], Hao Jing[4], Yongming Zhang[1,8], Zhishan Bo[2,9]*, and Feng Liu[1,3,8]**

[1]School of Chemistry and Chemical Engineering, Frontiers Science Center for Transformative Molecules, Shanghai Key Laboratory of Electrical Insulation and Thermal Aging, Shanghai Jiao Tong University, Shanghai 200240, China.

[2]College of Textiles & Clothing, State Key Laboratory of Bio-fibers and Eco-textiles, Qingdao University, Qingdao 266071, China.

[3]Suzhou Laboratory, Suzhou 215100, China.

[4]Shanghai OPV Solar New Energy Technology Co., Ltd., Shanghai 201210, China.

[5]Advanced light source, Lawrence Berkeley National Laboratory, Berkeley, CA 94720, USA.

[6]Materials Sciences Division, Lawrence Berkeley National Laboratory, Berkeley, CA 94720, USA.

[7]Polymer Science and Engineering Department, University of Massachusetts, Amherst, MA01003, USA.

[8]State Key Laboratory of Fluorinated Functional Membrane Materials and Dongyue Future Hydrogen Energy Materials Company, Zibo City, Shandong 256401, China.

[9]Beijing Key Laboratory of Energy Conversion and Storage Materials, College of Chemistry, Beijing Normal University, Beijing 100875, China.

[10]These authors contributed equally: Rui Zeng, Ming Zhang, Xiaodong Wang.

*e-mail: leizhu@sjtu.edu.cn, zsbo@bnu.edu.cn, fengliu82@sjtu.edu.cn

Abstract: Nonfused ring electron acceptors (NFREAs) represent a compelling class of *n*-type near infrared (NIR) photoactive semiconductors, distinguished by their pronounced molecular absorption and straightforward synthetic approaches. However, challenges such as diminished backbone planarity and the presence of bulky substituents adversely affect the crystallinity of NFREAs, thereby impeding charge transport and the formation of bicontinuous morphology in organic photovoltaic device. The solubility of donors and acceptors across various solvents is examined, revealing that solubility hysteresis can facilitate the formation of the highly crystalline donor polymer fibril, which in turn, refines the NFREA phase, thus inducing a better bicontinuous morphology with improved crystallinity. Leveraging these insights, a novel solubility hysteresis sequential condensation thin film fabrication methodology is devised, yielding photoactive layers of exceptional uniformity and smoothness. The well-defined interpenetrating network morphology afforded a record efficiency of 19.02%, as a marked advancement over conventional device fabrication methods. Additionally, a high efficiency retention (P_r) value of 92.3% is achieved in 1 cm^2 device (17.28% efficiency).

Introduction

Single-junction organic solar cells (OSCs) [1-4] based on conjugated polymer donors and fused ring electron acceptors (FREAs) [5-9] have achieved prominent power conversion efficiencies (PCEs) over 19% in recent years.[10-13] On the contrary, OSCs incorporating the more economically viable nonfused ring electron acceptors (NFREAs) [14-17] have been confined to efficiencies approximately 16%, suffering from low short-circuit current density (J_{SC}) and fill factor (FF). Unlike FREAs, NFREAs extend their backbone through C-C single bonds, circumventing the necessity for low-yield ring-closure reaction, thus typically offering simpler synthetic routes. However, the unfixed backbone geometry and weakened intermolecular r-r interaction are also originated. [18] Besides, NFREAs are similar with donor polymers in chemistry, which often leads to high material miscibility and unfavorably large mixing domains within blended photoactive film. Consequently, achieving a nano-sized interpenetrating network morphology with good crystallinity to meet the requirement of efficient exciton splitting and carrier transport is the forefront challenge for NFREA based OSCs.

In order to address the above-mentioned challenges, photoactive layer condensation strategy needs to be developed, aiming to mitigate intermolecular mixing and to introduce the formation of high-quality nano fibrillar network morphology within NFREA blends. The state-of-the-art NFREA 2BTh-2F-C_2 was utilized as the acceptor, 19 and D18 polymer as the donor to construct bulk heterojunction thin film. A combinatory solvent mixture was designed by looking into the vapor pressure and material solubility differences. Specifically, the solubility limit and non-equilibrium polymer chain assembly was designed to establish the polymer donor network and purify the acceptor phase, thus enhancing the phase separation and crystallization. Numerous solvent mixtures were studied and the donor/acceptor solubility hysteresis sequential condensation is developed. A generalized processing methodology is established, where the combination of a volatile good- solvent and a less-volatile bad-solvent for D18 is favored to instigate phase separation, allowing NFREA molecules to initially dissolve in the solvent mixture before segregating to form high-purity acceptor fibril phase in the residual solvent. Thus, during the first stage of film formation process, rapid evaporation of the volatile good solvent increases the concentration of the bad solvent, causing D18 to precipitate into form a gel-like fibrillar network. NFREA molecules subsequently crystallize slowly in-between the D18 fibril network as the bad-solvent volatilizes. Additionally, solid-state additive [20] is introduced, which resides in the nearly dried photoactive thin film to further enhance material crystallization. The crystallization processes of donor and acceptor materials are thus

distinguished and improved, contributing to improved interpenetrating morphology and carrier transport.

Based on the above-mentioned procedure, the chloroform (CF) and *o*-xylene (OXY) mixture emerged as superior for D18: 2BTh-2F-C_2 blends, which delivered a champion efficiency of 19.02% with a J_{SC} of 26.71 mA cm-2 and an FF of 77.98%, a significant advancement over conventional device preparation protocol. The solubility hysteresis sequential condensation methodology is successfully extended to multiple organic photovoltaic (OPV) blends that suffer from either pronounced intermolecular mixing or excessive phase separation. For NFREAs that are boasted of cost-effective synthesis, the performance-cost profit of the studied system reaches a high level with a figure-of-merit (FOM) of 28.3 (18.5 for PM6: Y6 blends). More importantly, the solubility hysteresis sequential condensation processing could manipulate solvent evaporation and mixture viscosity, which opens a large window for material deposition and surface flattening to reduce the area-induced efficiency loss. When the device area is extended to 1 cm^2, an efficiency of 17.28% is recorded, which is among the highest in 1 cm^2 OPV devices.

Results and Discussion

The Solubility Hysteresis Sequential Condensation Processing Methodology

The conventional OSC thin film morphology manipulation focuses on finite control of material crystallization and phase separation. However, many donor/acceptor mixtures, that are high miscibility or show strong tendency to segregate in bulk or on surface, are hard to be optimized even using ancillary additives. Such difficulties prevent us to fully explore the potential of organic photovoltaic materials, which are ideal photoactive absorbers spectrally and electronically but delivered poor device performances. Thus the approach in mattering blend morphology is in urgent needs for the quick emergence of new generation of photoactive materials. We take one step back to reconsider the morphology development of OSC thin film from solvent drying, and speculate that manipulating the photoactive material and solvent interaction to consequentially deposit donor and acceptor phase could lead to self-purified bicontinuous morphology in one shot. This avenue needs to design a solvent mixture that can result in solubility hysteresis, in which the solvent nature should deteriorate to bias out one phase while keep the other well solubilized. Thus solubility and volatility are the two major factors to be considered. The solubility parameter was calculated based on materials' chemical structure. [21] The solvents considered include CF, carbon tetrachloride (CTC),

toluene (TL), OXY, trimethylbenzene (TYL), chlorobenzene (CB), *o*-dichlorobenzene (ODCB), bromobenzene (BrB), *o*-dibromobenzene (ODBrB), tetrahydrofuran (THF), methyltetrahydrofuran (MTHF), and dibromothiophene (DBTh), as shown in Fig. 1a. The calculated atomic dispersive interactions (δ_D), permanent dipole molecular interactions (δ_P) and molecular hydrogen bonding interactions (δ_H) are summarized in Supplementary Table 1. The parameter δ_V is introduced since that δ_D and δ_P show similar dissolution effect.22

$$\Delta_1 = \sqrt{\delta_{D1}^2 + \delta_{P1}^2} \quad (1)$$

δ_H is important when polar interaction exists, which is considered as the other key interaction towards material solubilization. As shown in Fig. 1b, a 2-dimensional solubility matrix for D18 based on δ_H and δ_V was constructed, where the different interacts that affect material solubility can be effectively visualized.[21] A solubility circle that summarizes the solubility parameter differences

between target material and solvent are constructed with a radius of R_a,21 as follow

$$\Delta_a = \sqrt{\Delta\delta_D^2 + \Delta\delta_H^2} \quad (2)$$

The relative energy difference (*RED*) index is introduced, which is defined as

$$RED = R_a/R_0 \quad (3)$$

The solubility region of polymers in common is approximately limited within a circle with a radius of about 5 δ-units (solubility sphere with $R_0 = 5$).21, 23 Good solvents show a *RED* index smaller than 1, which are inside the solubility sphere. Bad solvents have a *RED* index larger than 1, and the larger the *RED* number, the worse the solubility. The *RED* index of different systems is summarized in Supplementary Table 2.

The validity of *RED* index is examined by the absorption spectra (Fig. 1c). D18 in good solvent shows an absorption maximum ~ 575 nm, and over than 40 nm red-shift is seen for absorption in bad solvent, which indicates chain aggregation in bad solvent. We then measured the laser light path for different solutions (Supplementary Fig. 1). Tyndall effect can be observed for TL, OXY and TYL solutions, suggesting D18 gel-like aggregation due to poor solubility. Diffusive light path was seen for MTHF solution, suggesting the presence of large particles in solution. This is due to the extremely poor solubility of D18 in MTHF, which makes the aggregation unable to be controlled. The time-dependent optical transmittance measurement was carried out for D18 MTHF, OXY and CB dilute solution (Supplementary Fig. 2). High transmittance of MTHF solution in 460-640 nm region suggests that large amount of D18 precipitates out and the solution concentration is low (~1/3 comparing to the concentration of CB

and OXY solutions). Transmittance in 680-700 nm region is

related to Tyndall diffraction in light path. The transmittance of CB solution remains quite stable during ~2 h solution aging. MTHF solution transmittance changes largely, suggesting prominent aggregation growth. Transmittance of OXY solution shows weak aggregation growth without material precipitation. The limited solubility and slower aggregation growth of OXY solution open a controllable time window for thin film morphology manipulation. Supplementary Fig. 3 illustrates the Tyndall effect measurement for 2BTh-2F-C_2 in various solution. The absence of a visible laser light path suggests that no gel-like aggregation occurs in any of the solvents tested. Therefore, it can be inferred that the small molecule nonfused ring electron acceptors 2BTh-2F-C_2 could be effectively solubilized in the studied solvents. The normalized UV-vis absorption for 2BTh-2F-C_2 in various solvents as shown in Supplementary Fig. 4, align well with the calculated solubility parameters.

We then studied the vapor pressure of selected solvents (Supplementary Table 2), which determines the evaporation sequence from the mixed solvent. This feature in coupling with *RED* index establishes a four quadrant solution property map (Fig. 1d). For the D18 donor polymer, CF and CTC are volatile good solvent; THF and MTHF are volatile bad solvent; CB, ODCB, BrB, ODBrB, DBTh are low-volatile good solvent; and, TL, OXY and TYL are low-volatile bad solvent. A combination of volatile good solvent and low-volatile bad solvent results in a dynamic solution mixture that solubility towards D18 deteriorates gradually, and thus polymer aggregation can be controlled. The CF&OXY mixture is taken as an example to study the volatilization mechanism.

For the CF&OXY binary solution, the vapor pressure is given by Raoult's law[24]:

$$P^{O} = \frac{P}{n_{CF}/(n_{CF}+n_{OXY})} \quad \text{or} \quad \frac{P}{n_{OXY}/(n_{CF}+n_{OXY})} \tag{4}$$

where P^O is the vapor pressure, P is the partial vapor pressure, and n is the amount-of-substance defined by $n = m/M$, where ρ is the density, V is the volume, and M is the molar mass. The vapor pressure as the function of volume fraction is shown in Fig. 1e. Thus, CF serves as the solubilizing agent and quickly removes to transfer donor/acceptor materials into OXY dominated solution. The thin film drying kinetics is shown in Supplementary Fig. 5. It is seen that CF solvent vaporizes

within seconds and then OXY removal kinetic dominates (red). The OXY solution shows two distinctive removal slopes (blue). The first slope is the evaporation of free OXY in solution, and

the second slope is the slow removal of OXY that is associated with gel-type aggregation. The removal of OXY in CF&OXY shows a slop less steep comparing to free OXY removal, which suggests a

more controllable gel-type aggregation formation. To make an appropriated solvent mixture to fully induce D18 fibril-like aggregation, the OXY concentration should be set over the deflection point in OXY solution removal profile (~8% of the total thickness of OXY wet film). And in the current case, an 12% of OXY in CF&OXY is found to be optimal. In nature, D18 chain starts to assemble into fibrils after CF evaporation. Upon the continuous removal of OXY residual solvent, solubility limit forces more D18 to precipitate in an unrushed manner to form fibril network. Meanwhile, the mobile phase is enriched with 2BTh-2F-C_2 and gradually phase purified. The primary D18 network phase dictates the morphology, and then 2BTh-2F-C_2 molecules order within the D18 fibril mesh to form secondary 2BTh-2F-C_2 network. Thus material crystallization is enhanced and mixing domain size is reduced, and the length scale of phase separation is mostly dictated by the size of the fibril diameter. This processing explores the solubility hysteresis to induce consequential fibril formation can be of high advantage for solar cell devices since the crystallization is enhanced in balance.

Last but not the least, solid additive of 1,4-diiodobenzene (DIB) [25-26] as shown in Supplementary Fig. 6a can be introduced and set as the last removal agent to further enhance material crystallization. As shown in Supplementary Fig. 6b and Supplementary Table 3, the film thickness decline by ~22 nm after annealing, indicating the existance of DIB until thermal annealing. During the film formation process, the progressive evaporation of CF results in a notable elevation of DIB concentration within OXY, which interacts with the acceptors in the last stage to regulate the morphology of the NFREAs and balance the charge transport. Supplementary Fig. 6c shows the normalized absorption for 2BTh-2F-C_2 precursor solution with or without solid additive of DIB. The absorption of 2BTh-2F-C_2 shows red-shift after adding DIB, suggesting a slightly planarization of molecular conformation of acceptor under the presence of DIB. This feature could induce better ordering of 2BTh-2F-C_2 during film formation. 13 The Time of Flight Secondary Ion Mass Spectrometry (TOF-SIMS) measurement is performed to further investigate the effect of DIB on the distribution of D18 and 2BTh-2F-C_2 in the final film (Supplementary Fig. 7). The unique cyanide (CN^-) is used to trace the acceptor 2BTh-2F-C_2. It is observed that 2BTh-2F-C_2 molecules exhibit a propensity for shallow surface accumulation in the film under DIB conditions. This suggests that the migration of some 2BTh-2F-C_2 molecules towards the film surface occurs during the DIB departure process due to strong interaction. These findings demonstrate the

advantageous role of DIB in optimizing the vertical distribution within the D18:2BTh-2F-C_2 film.

The influences

of DIB on crystallization are complemented as shown in Supplementary Fig. 8 and Supplementary Table 4-5. The obvious peak intensity enhancement is seen for the DIB condition, presenting an orderly arrangement in the D18:2BTh-2F-C_2 film after DIB treatment. The CCLs and peak areas for the lamellar packing (IP profiles) are 99.05, 110.5 Å, and 1.45, 2.55 for w/o DIB and DIB processed blends, respectively. And for π-π stacking (OOP profiles), the CCLs and peak areas are 18.98, 20.95 Å, and 3.07, 3.29 for w/o DIB and DIB processed blends, respectively. Thus, the introduction of solid additive DIB is benefited to the optimization for the crystallization morphology. The mechanism of solubility hysteresis sequential condensation processing is examined by *in-situ* UV–vis absorption spectroscopy (Fig. 1f-h, Supplementary Fig. 9, Supplementary Table 6). [27-29] The 520 nm absorption and the 790 nm absorption are used to track the ordering of D18 and 2BTh-2F-C_2. D18 and 2BTh-2F-C_2 order quickly in CF solution (~500 ms) and slowly in OXY solution (~44.5 s) from a fully solubilized condition. The ordering transition is quite steep (Supplementary Fig. 10) and simultaneously, offering a limited window for morphology optimization. In CF&OXY solution, D18 gradually orders in-between 500-3500 ms, and 2BTh-2F- C_2 orders at ~4000 ms. Thus the D18 gel-like framework is gradually formed and 2BTh-2F-C_2 is kept in mobile phase. 2BTh-2F-C_2 ordering occurs in-between D18 network in later stage of film drying, thus phase purity and crystallinity can be enhanced. These results are fully consistent with the Raoult's calculation (Fig. 1e) and *in-situ* thickness measurement (Supplementary Fig. 5). The schematic illustration of the mechanism for the evolution process is shown in Supplementary Fig. 11.

Photovoltaic Device Performance and Cost Advantage Analysis

The solar cell device performance of NFREA is strongly affected by the difficulties in obtaining a suitable bicontinuous morphology. 2BTh-2F-C_2 is one of the best-performing NFREA acceptor with reported efficiency only of 15.4%. [19] Poor phase separation and low crystallinity are the major reasons that limit J_{SC} and FF. Using the optimized solubility hysteresis sequential condensation device fabrication method, significant improvement in device performance are recorded. The *J-V* curves and solar cell performances are summarized in Fig. 2a, Table 1, Supplementary Fig. 12-13, and Supplementary Table 7-8. The CF, OXY and CF&OXY processed

solar cells showed a PCE of 15.59% (V_{OC} = 0.915 V, J_{SC} = 24.53 mA cm−2, FF = 69.49%), 17.50% (V_{OC} = 0.911 V, J_{SC} = 25.68

mA cm−2, FF = 74.83%) and 19.02% (V_{OC} = 0.913 V, J_{SC} = 26.71 mA cm−2, FF = 77.98%), respectively. Certified PCE reaches 18.63% (Supplementary Fig. 14), which is the highest value for NFREA based solar cells. The higher J_{SC} and FF in CF&OXY device indicate both carrier generation and carrier transport are optimized, which suggests a more favorable bicontinuous morphology is obtained. The external quantum efficiencies (EQEs) and differences are shown in Fig. 2b and Supplementary Fig. 15. The EQE in 350-450 nm is mainly from D18, and that in 700-850 nm is mainly from 2BTh-2F-C_2 film (Supplementary Fig. 16). Thus, compared with CF and OXY processed device, solar cells fabricated using CF&OXY solvent mixture show improved EQE in both donor and acceptor region, with higher contribution from NFREA absorption region. Thus the solubility hysteresis sequential condensation processing solved difficulty in constructing a continuous high mobility acceptor phase, which is accredited to the improved NFREA crystallization in OXY residual solvents. Fig. 2c summarized the statistical PCE prepared by different solvent conditions, which demonstrates a good reproducibility of device performance. An explicit comparison to the state-of-the-art NFREAs performance is shown in Fig. 2d and Supplementary Fig. 17a based on the current results and the another 78 data points from 55 literatures (detailed data shown in Supplementary Table 9). The major difficulty to achieve a high efficiency for NFREA blends is that V_{OC}*FF value drops at high J_{SC} level, as seen from the regression analysis in Supplementary Fig. 17b. The device fabrication method can jump out of this limitation, which sets the records for NFREA solar cells.

Considering both synthetic complexity (SC, Supplementary Fig. 18-21) and PCE, the cost-efficiency was analyzed, and the figure of merit (FOM) [30-31] was calculated by

$$\mathrm{FOM} = \mathrm{PCE/SC} \tag{6}$$

Fig. 2e shows the macroscopic factors matrix, with detailed parameters summarized in Supplementary Table 10-11. The FOM value of 2BTh-2F-C_2 reaches 28.3, which is well above many widely used acceptors such as IT-4F (23.9), Y6 (18.5), and L8-BO (18.7). Solar cell device performances using other solvent combinations are shown in Fig. 2f and Supplementary Table 12-13). This PCE map clearly suggests the mixture of volatile good solvent and low-volatile bad solvent processing is effective but to different extent. An additional set of universal applicability experiment based on different NFREAs (molecular structures shown in Supplementary Fig. 22) is executed. The device performance is shown in Supplementary Table 14 and Supplementary Fig. 23, which

generally exhibits a good improvement. We have tried solubility hysteresis sequential condensation processing in the most studied OPV blends with results shown in Supplementary Table 15 and Supplementary Fig. 24. We find that the optimal OXY content increases from 12% to 25% (Supplementary Fig. 25 and Supplementary Table 16) due to the different properties of the polymer material. This is an important reason for less improvement in previous experiments, and the representative combination (PM6:Y6, PM6:eC9) are supplemented in optimal condition shown in Supplementary Table 15. Meanwhile, the intrinsic characteristics of the materials also determine its improvement limitation. Differences in solubility and crystallinity whittle its potential for optimization. As additional obvious illustration, it should also be noted that slight PCE reduction are seen in PM6:PY-IT and PTB7-Th:IEICO-4F systems, which are contrary to solvent strategy principles since relatively small solubility differences (between PM6 and PY-IT) and insufficient polymer crystallization (PTB7-Th). Considering the effect of polymer batches on performance, the D18 with different number-average molecular weights (M_n) was used as shown in Supplementary Table 17 and Supplementary Fig. 26. The M_n of these D18 polymers is characterized by Gel Permeation Chromatography (GPC) characterization as shown in Supplementary Fig. 27. It is seen that the device performance is progressively increased as the molecular weight of D18 escalates from approximately 2W to 6W for devices fabricated using CF solvent. However, for OXY solution device fabrication, the device performance decreases when molecular weight increase, which is due to the reduced solubility of larger molecular weight D18 that fibrillar assembly is hard to optimize. A marked decrease in solubility in OXY solvent is noted as the molecular weight of D18 approaches 5W, and when the molecular weight reaches ~6W, D18 exhibits significant processing challenges with OXY solvent, culminating in a substantial deterioration in device performance. These effects lead to limited molecular weight to be used in CF&OXY solvent mixture. Actually, for different molecular weighted D18, the optimal solvent mixture composition should also change. For the current CF&OXY recipe, the optimal PCE is obtained when employing D18 with M_n of around 4W, where D18 exhibits an effective balance between its processability and hole transport characteristics.

Charge Transfer and Transport Analysis

The spectral and temporal characteristics of the charge-transfer dynamics in the blended thin films were studied using the transient absorption spectroscopy (TAS). [32-36] The excitation

wavelength of 800 nm was used to excite 2BTh-2F-C_2 only. The 2D spectra and representative TAS profiles at indicated delay times are shown in Supplementary Fig. 28. The decay traces at ~800 nm represent the ground-state bleach (GSB) of 2BTh-2F-C_2, and the decay traces at around 940 nm are assigned to excited states absorption (ESA) of 2BTh-2F-C_2. With the decay of the 2BTh-2F-C_2 bleach peak (800 nm), the D18 GSB peak at around 595 nm rises, suggesting the hole-transfer process from 2BTh-2F-C_2 to D18. Fig. 3a shows the hole-transfer process profiles, and Supplementary Table 18 summarizes the kinetics parameters fitted by biexponential function. The fast components (τ_1) represent the kinetics of the exciton dissociation in mixing domain or at interfaces, which are 1.16, 1.10 and 0.92 ps for the CF, OXY, and CF&OXY processed blends. The slow components (τ_2) represent the kinetics of exciton diffusion in crystalline domain to interfaces, which are 24.06, 22.14 and 19.01 ps for the CF, OXY, and CF&OXY processed blends. The faster hole-transfer in mixing region in CF&OXY processed blends suggests a more favorable D-A interaction, and the faster diffusion in NFREA domain suggests better interpenetrating crystalline network structure inherited from the sequential crystallization.

Space-charge-limited current (SCLC) measurement was performed and the results are shown in Supplementary Fig. 29 and Fig. 3b. It is seen that both the electron mobility (μ_e) and hole mobility (μ_h) for OXY-device are improved compared with CF-device. And for CF&OXY-device, the μ_e and μ_h are improved significantly in balanced manner. The μ_e/μ_h value of CF, OXY, CF&OXY based device are calculated to be 0.41, 0.43, 0.84, respectively. The largely improved μ_e results in high EQE in NFREA absorption region. The carrier collection efficiency P(E, T) values are 95.8%, 96.2%, and 97.3%, respectively, for the CF, OXY, and CF&OXY based device derived from photocurrent density-effective voltage (J_{ph}-V_{eff}) characterization (Fig. 3c), and a much higher drifting current is seen in low V_{eff} region. These results suggest well developed bicontinuous network of CF&OXY processed thin film.

The charge transport and recombination were investigated by transient photovoltage (TPV) and transient photocurrent (TPC) measurements. 37 The fitted charge lifetimes (τ_c) and charge density (n) under different V_{OC} conditions are summarized in Supplementary Fig. 30. Both τ_c and n for CF&OXY devices show higher value than those in the other devices over the applied V_{OC} region, which is ascribed to reduced charge recombination, suggesting less defects and traps in

CF&OXY

processed device. The charge lifetime as a function of charge density is shown in Fig. 3d, which follows an approximately exponential law of

$$\tau_1 = \tau_0(\cdot)^2 \quad (7)$$

where 1_0 and n_0 are constants, and the exponential factor 11 is in relation to the non-geminate recombination order R (R=11+1, and R = 2 in ideal condition). The CF&OXY device shows a minimum R of 2.06 with the maximum lifetimes, which indicates minimized non-geminate recombination. Similar conclusions can be drawn from light intensity (P_{light})-dependent J_{SC} and V_{OC} measurements (Supplementary Fig. 31 and Supplementary Table 19). The non-geminate

recombination rate coefficient $k(n)$ follows the equation of

$$k(n) = \frac{3}{4\pi(\cdot)\times} \quad (8)$$

where $\tau_c(n)$ is the carrier lifetime. The $k(n)$ as a function of charge densities is shown in Fig. 3e, 38 also confirming suppressed recombination in CF&OXY processed device.

The fundamental semiconductor properties of the blended thin films were studied by the electron density of state (DOS) characterization, following the relationship of [39]

$$g(E) = \frac{N_t}{E_t}\exp\left(-\frac{E-E_{LUMO}}{E_t}\right); \quad (9)$$

where N_t is the total density per unit volume, E_{LUMO} is the LUMO energy level, and E_t is the energy for exponential tail distribution that describes energetic disorder. As shown in Fig. 3f, the CF device shows a N_t of 1.374×1019 cm−3 eV−1 and an E_t of 72.4 meV. The CF&OXY device shows a much larger N_t of 5.396×1019 cm−3 eV−1 and a smaller E_t of 63.1 meV, indicating a higher and narrower DOS distribution. The device N_t agrees well with the n value obtained in TPC/TPV measurement, validating that the increased charge density is the major contribution to the J_{SC} improvement in CF&OXY devices.

Thin Film Morphology Characterization

Thin film morphology from conventional and solubility hysteresis sequential condensation processing was studied by various imaging and scattering techniques. The atomic force microscopy- based infrared spectroscopy (AFM-IR) measurement was used to investigate the key feature of 2BTh-2F-C_2 phase in blend film by using the specific Fourier transform infrared (FT-IR) spectroscopy at 1700 cm^{-1} (Supplementary Fig. 32). [40-42] As shown in Fig. 4a-c, CF processed thin film is high homogenous, and the specific IR band cannot be found well developed 2BTh-

2F-C_2

phase. OXY processed thin film shows distinctive fibril morphology with an average diameter of 20.5 nm (extracted from AFM-IR linecut in Supplementary Fig. 33). CF&OXY processed thin film also displays fibril morphology with diameter increased to 25.9 nm. Thus the advantage of solubility hysteresis sequential condensation processing in inducing 2BTh-2F-C_2 assembly is obvious. It should be noted that OXY has a very limited solubility for D18, and blended thin film needs to be processed when solution is still hot. CF&OXY solution is much easier to handle and reproducible, and the dynamic solution quality deterioration via consequential evaporation could better induce a bicontinuous phase separation for NFREA blends.

We then quantitatively analyzed the blended thin film crystallization using grazing incidence wide-angle X-ray scattering (GIWAXS). [43] The scattering patterns and the sector averaged profiles in the in-plane (IP) and out-of-plane (OOP) directions are shown in Supplementary Fig. 34-36. Fig. 4d underlined the difference of crystallization behavior under different processing methods. The

~0.3 $Å^{-1}$ and ~1.7 $Å^{-1}$ peaks are from the lamellae packing and TC-TC stacking of both donor and acceptor. Comparing with the CF processed blends, peak intensity enhancement is seen for OXY and CF&OXY processed thin film. The crystalline coherence lengths (CCLs) and peak areas for the lamellar packing (IP profiles, Supplementary Tables 20-21) are 100.9, 105.8, 113.4 Å, and 55.93, 69.03, 78.19 for CF, OXY, and CF&OXY processed blends, respectively. And for TC-TC stacking (OOP profiles), the CCLs and peak areas are 19.55, 19.87, 21.33 Å, and 102.14, 233.85, 263.35 for CF, OXY, and CF&OXY blends, respectively. Paracrystalline disorder factor (g-factor) for TC-TC stacking peak [44-45] is also calculated (Supplementary Table 21) to evaluate structure order difference, where the g-factor of 17.4%, 17.1%, 16.6% are obtained for the CF, OXY, CF&OXY processed thin films. These results confirm that the solubility hysteresis sequential condensation processing could enhance the ordering of TC-TC stacking more effectively, which solves the fundamental limitation of weak ordering of NFREA in photoactive blends.

We then studied the blend solution state assembly by using the cryogenic transmission electron microscopy (cryo-TEM). Fig. 4e-f show the cryo-TEM images of CF, OXY, CF&OXY solution. The lattice structure of D18 is seen, with the inter-planar distance of ~2 nm, which is from lamellae chain packing. In CF, the pre-ordering is weak, and solution is thus stable. For OXY solution, the solution assembly is much more complicated. D18 can only be solubilized in hot solution (above 120 °C), and under quick liquid ethylene freezing sample preparation, polymer

chains get frustrated

and aggregated into nanospheres with less optimal lamellae packing. The CF&OXY solution takes the double-folded advantages, prominent lamellae packing is seen with no nanosphere aggregation. And in the film formation process, these lamellae packing can be further developed into larger fibrils in remaining OXY. The phase images and height images of atomic force microscopy (AFM), and transmission electron microscope (TEM) images for CF, OXY, CF&OXY based blend films are shown in Supplementary Fig. 37. A fibrillar morphology is more pronounced in CF&OXY processed thin film. These results indicate that using solubility hysteresis sequential condensation method to induce differential material assembly with a controllable kinetics is optimal in driving the bicontinuous morphology of OPV blends. And the two step crystallization could better enhance the crystallinity and phase connectivity, arresting interpenetrating network with limited length scale and better conductivity.

Large-Area Device Fabrication

It is found that the performance uniformity of different device pixels at different locations on device substrate varies greatly, which is due to the thin film thickness uniformity. The thickness distribution of the CF, OXY, and CF&OXY processed thin films are characterized on wafer substrate. As shown in Fig. 5a, we measured the point thickness in line across wafer center (2 mm apart for each), and the detailed data are summarized in Supplementary Table 22. We then measured the surface profile with 2*2 mm size scale focusing the point center using optical profilemeter (Supplementary Fig. 38). Thickness variation ~2.5 nm is recorded for CF&OXY, which is much smaller comparing CF and OXY condition. The surface roughness (S_a) extracted from surface profile are 11.61, 9.18, 4.47 nm for CF, OXY, CF&OXY processed films, respectively. Thus solubility hysteresis sequential condensation processing could afford highly uniform and smooth thin film, which is essential for large area device fabrication. This advantage originates from the unique rheological behaviors of polymer assembly in CF&OXY solution. The rheological measurement [46-47] was performed on D18 in CB and OXY solutions (CF is too volatile to conduct rheological measurement). The viscosity (ri) and shear stress (a) for OXY solution is about one order of magnitude larger comparing to CB solution (Fig. 5b). This is due to the fibrillar aggregation of D18 in OXY solution (see Fig. 1c and Supplementary Fig. 1), which leads to network structure and high viscosity. In fact in higher concentration (~5 mg mL^{-1}), a weak gel state could be formed.

Due to the high *ri* and *a*, the OXY solution spin coating results in thick edges under centrifugal force. CF solution is in low viscosity and high volatility, which leads to thicker film in the middle. As for CF&OXY binary solution, the sequential deposition results in unique advantage. The low viscosity leads to quick spreading of solution, and then the quickly elevated viscosity suppresses multiple instabilities to afford flat and smooth thin film. Fig. 5c shows the thickness and efficiency statistics of the device processed from CF, OXY, and CF&OXY solvents. At different position on a device substrate, the thickness variation of CF-device is significant, and that of CF&OXY-device is quite uniform. Such uniformity is directly related with device performance. Supplementary Table 23 shows the detailed performance *vs.* thickness in CF, OXY, and CF&OXY processed device (ten pixels on each device substrate with sample configuration shown in certification report page 6-7).

We then fabricate large area solar cell devices (1 cm^2) [48-49] to evaluate the performance drop comparing to small area devices (5.2 mm^2). As seen from Fig. 5d and Supplementary Table 24, the PCEs of 5.2 mm^2 device for CF, OXY, CF&OXY fabrication are 15.38%, 17.36%, 18.72%, respectively. And the PCEs of 1 cm^2 device for CF, OXY, CF&OXY fabrication are 11.67%, 14.86%, 17.28%, respectively. The efficiency retention factor (P_r), the PCE ratio of large-area device to small-area device, is used to evaluate the quality factor on device area. The P_r values for CF, OXY and CF&OXY solution processed devices are 75.9%, 85.6% and 92.3%, respectively (Fig. 5e and Supplementary Table 25). The optimal morphology and uniformity correlate with low series resistance (R_s) and high shunt resistance (R_{sh}), 50-51 thus better electrical property is obtained to deliver a high P_r value for CF&OXY.

Conclusion

To conclude, the solubility hysteresis sequential condensation strategy for organic solar cell fabrication emerges as a groundbreaking solution to the challenge of bicontinuous morphology optimization for NFREA blended thin film. The optimized donor/acceptor interpenetrating network with enhanced crystalline quality results in highly efficient and balanced charge transfer and transport properties. And champion efficiency of 19.02% (certified as 18.63%) is obtained with much better performance-cost benefits. More importantly, solubility hysteresis sequential condensation fabrication could produce the film with better thickness uniformity and smoothness, and thus the efficiency drop is much smaller when scaling the device area from 5.2 mm^2 to 1 cm^2.

The best efficiency of CF&OXY processed NFREA 1 cm^2 large-area device is 17.28%, maintaining 92.3% of the initial value in 0.052 cm^2 area device. These results are highly encouraging, demonstrating a harmonious integration of performance, cost, and scalability under the solubility hysteresis sequential condensation solar cell fabrication paradigm, signifying a bright future for commercial application.

Data availability

The data that support the plots within this paper and other findings of this study are available from the corresponding authors upon request. The raw data has been uploaded to the database. Source data are provided with this paper in the Materials Cloud database (DOI: 10.24435/materialscloud:nt- y8).

References

1. Cheng, P., Yang, Y. Narrowing the band gap: The key to high-performance organic photovoltaics. *Acc. Chem. Res.* **53**, 1218-1228 (2020).
2. Zhao, Y. et al. Achieving sustainability of greenhouses by integrating stable semi-transparent organic photovoltaics. *Nat. Sustain.* **6**, 539–548 (2023).
3. Meng, D. et al. Near-infrared materials: the turning point of organic photovoltaics. *Adv. Mater.* **34**, 2107330 (2022).
4. Shen, W., Zhao, Y., Liu, F. Highlights of mainstream solar cell efficiencies in 2022. *Front. Energy* **17**, 9–15 (2023).
5. Cheng, H. W., Zhao, Y., Yang, Y. Toward high-performance semitransparent organic photovoltaics with narrow-bandgap donors and non-fullerene acceptors. *Adv. Energy Mater.* **12**, 2102908 (2022).
6. Cheng, P., Li, G., Zhan, X., Yang, Y. Next-generation organic photovoltaics based on non-fullerene acceptors. *Nat. Photon.* **12**, 131–142 (2018).
7. Huang, C. et al. Highly efficient organic solar cells based on S, N-heteroacene non-fullerene acceptors. *Chem. Mater.* **30**, 5429-5434 (2018).
8. Shi, X. et al. Design of a highly crystalline low-band gap fused-ring electron acceptor for high-efficiency solar cells with low energy loss. *Chem. Mater.* **29**, 8369-8376 (2017).
9. Zhang, M. et al. High-efficiency organic photovoltaics using eutectic acceptor fibrils to achieve current amplification. *Adv. Mater.* **33**, 2007177 (2021).
10. Fu, J. et al. 19.31% binary organic solar cell and low non-radiative recombination enabled by non-monotonic intermediate state transition. *Nat. Commun.* **14**, 1760 (2023).
11. Zhu, L. et al. Single-junction organic solar cells with over 19% efficiency enabled by a refined double-fibril network morphology. *Nat. Mater.* **21**, 656-663 (2022).
12. Zhang, M. et al. Single-layered organic photovoltaics with double cascading charge transport pathways: 18% efficiencies. *Nat. Commun.* **12**, 309 (2021).
13. Zeng, R. et al. All-polymer organic solar cells with nano-to-micron hierarchical morphology and large light receiving angle. *Nat. Commun.* **14**, 4148 (2023).
14. Wang, X. et al. A simple nonfused ring electron acceptor with a power conversion efficiency over 16%. *Chin. J. Chem.* **41**, 665-671 (2023).

15. Zheng, X. et al. Simple non-fused ring electron acceptors with well-controlled terminal group stacking. *Cell Rep. Phys. Sci.* **3**, 101169 (2022).
16. Ma, D., Zhang, Q., Li, C. Unsymmetrically chlorinated non-fused electron acceptor leads to high-efficiency and stable organic solar cells. *Angew. Chem. Int. Ed.* **5**, e202214931 (2022).
17. Ma, L. et al. Completely non-fused electron acceptor with 3D-interpenetrated crystalline structure enables efficient and stable organic solar cell. *Nat Commun*. **12**, 5093 (2021).
18. Meng, D. et al. Noncovalent π-stacked robust topological organic framework. *Proc. Natl. Acad. Sci. USA* **117**, 20397-20403 (2020).
19. Wang, X. et al. Simple nonfused ring electron acceptors with 3D network packing structure boosting the efficiency of organic solar cells to 15.44%. *Adv. Energy Mater.* **11**, 2102591 (2021).
20. Fan, B. et al. Understanding the role of removable solid additives: Selective interaction contributes to vertical component distributions. *Adv. Mater.* **35**, 2302861 (2023).
21. Krevelen, D. W., Nijenhuis, K. Properties of polymers, pp. 209-219. Elsevier Press, Netherlands (2009).
22. Bagley, E. B., Nelson, T. P., Scigliano, J. M. Three-dimensional solubility parameters and their relationship to internal pressure measurements in polar and hydrogen bonding solvents. *J. Paint Technol.* **43**, 35-42 (1971).
23. Hansen, C. M. Polymer additives and solubility parameters. *Prog. Org. Coat.* **51**, 109-112 (2004).
24. Liron, Z., Srebrenik, S., Martin, A., Cohen, S. Theoretical derivation of solute-solvent interaction parameter in binary solution: Case of the deviation from Raoult's Law. *J. Pharm. Sci.* **75**, 463-468 (1986).
25. Fu, J. et al. Eutectic phase behavior induced by a simple additive contributes to efficient organic solar cells. *Nano Energy* **84**, 105862 (2021).
26. Xie, Y. et al. High-efficiency organic solar cells enabled by an alcohol-washable solid additive. *Sci. China Chem.* **64**, 2161-2168 (2021).
27. Li, F. et al. Hydrogen-bond-bridged intermediate for perovskite solar cells with enhanced efficiency and stability. *Nat. Photon.* **17**, 478–484 (2023).
28. Liu, M. et al. Compact hole-selective self-assembled monolayers enabled by disassembling micelles in solution for efficient perovskite solar cells. *Adv. Mater.* 2304415 (2023).

29. Bi, L. et al. Deciphering the roles of MA-based volatile additives for α-FAPbI3 to enable efficient inverted perovskite solar cells. *J. Am. Chem. Soc.* **145**, 5920-5929 (2023).
30. Zhou, Y. et al. High-efficiency organic solar cells based on a low-cost fully non-fused electron acceptor. *Adv. Funct. Mater.* **31**, 2101742 (2021).
31. Guo, J. et al. 15.71% efficiency all-small-molecule organic solar cells based on low-cost synthesized donor molecules. *Adv. Funct. Mater.* **32**, 2110159 (2022).
32. Zhou, G. et al. Marcus hole transfer governs charge generation and device operation in nonfullerene organic solar cells. *ACS Energy Lett.* **6**, 2971-2981 (2021).
33. Zhou, G. et al. Spontaneous carrier generation and low recombination in high-efficiency non-fullerene solar cells. *Energy Environ. Sci.* **15**, 3483-3493 (2022).
34. Jiang, K. et al. Suppressed recombination loss in organic photovoltaics adopting a planar–mixed heterojunction architecture. *Nat. Energy* **7**, 1076–1086 (2022)
35. Xue, J. et al. A small-molecule "charge driver" enables perovskite quantum dot solar cells with efficiency approaching 13%. *Adv. Mater.* **31**, 1900111 (2019).
36. Wang, M. et al. Rational selection of the polymeric structure for interface engineering of perovskite solar cells. *Joule* **6**, 1032-1048 (2022).
37. Hamilton, R. et al. Recombination in annealed and nonannealed polythiophene/fullerene solar cells: transient photovoltage studies versus numerical modeling. *J. Phys. Chem. Lett.* **1**, 1432-1436 (2010).
38. Lin, B. Q. et al. Multiple-band linear-polarization conversion and circular polarization in reflection mode using a symmetric anisotropic metasurface. *Phys. Rev. Appl.* **9**, 024038 (2018).
39. Blakesley, J. C., Neher, D. Relationship between energetic disorder and open-circuit voltage in bulk heterojunction organic solar cells. *Phys. Rev. B* **84**, 075210 (2011).
40. Li, F. et al. Plasmonic local heating induced strain modulation for enhanced efficiency and stability of perovskite solar cells. *Adv. Energy Mater.* **12**, 2200186 (2022).
41. Zhao, Y. et al. A polymerization-assisted grain growth strategy for efficient and stable perovskite solar cells. *Adv. Mater.* **32**, 1907769 (2020).
42. Wang, R. et al. Caffeine improves the performance and thermal stability of perovskite solar cells. *Joule* **3**, 1464-1477 (2019).
43. Song, J. G. et al. Morphology characterization of bulk heterojunction solar cells. *Small Methods* **2**, 1700229 (2018).

44. Noriega, R. et al. A general relationship between disorder, aggregation and charge transport in conjugated polymers. *Nat. Mater.* **12**, 1038–1044 (2013).

45. Peng, Z., Ye, L., Ade, H. Understanding, quantifying, and controlling the molecular ordering of semiconducting polymers: from novices to experts and amorphous to perfect crystals. *Mater. Horiz.* **9**, 577-606 (2022).

46. Hao, B., Li, B., Yu, W. Nonequilibrium structure diagram of pendular suspensions under large-amplitude oscillatory shear. *Langmuir* **37**, 6208-6218 (2021).

47. Hao, B., Yu, W. A new solid-like state for liquid/liquid/particle mixtures with bicontinuous morphology of concentrated emulsion and concentrated suspension. *Langmuir* **35**, 9529-9537 (2019).

48. You, J. et al. A polymer tandem solar cell with 10.6% power conversion efficiency. *Nat. Commun.* **4**, 1446 (2013)

49. Fu, H. et al. 16.3% Efficiency binary all-polymer solar cells enabled by a novel polymer acceptor with an asymmetrical selenophene-fused backbone. *Sci. China Chem.* **65**, 309–317 (2022).

50. Luke, J. et al. A commercial benchmark: light-soaking free, fully scalable, large-area organic solar cells for low-light applications. *Adv. Energy Mater.* **11**, 2003405 (2021).

51. Chaudhary, D. K., Dhawan, P. K., Patel, S. P., Bhasker, H. P. Large area semitransparent inverted organic solar cells with enhanced operational stability using TiO2 electron transport layer for building integrated photovoltaic devices. *Mater. Lett.* **283**, 128725 (2021).

Acknowledgments

F. L. and L.Z. and M.Z. acknowledge the financial support from the National Natural Science Foundation of China (grant nos 52325306, 22379094 and 22309111), the National Key R&D Program of China (grant nos 2020YFB1505500, 2020YFB1505502), the Program of Shanghai Science and Technology Commission science and technology innovation action plan (grant nos 20ZR1426200, 20511103800, 20511103802 and 20511103803), the Natural Science Foundation of Shandong Province (grant no ZR2019LFG005), the Key research project of Shandong Province (grant no 2020CXGC010403), the Center of Hydrogen Science, Shanghai Jiao Tong University, China. Z. B. and Y. L. acknowledge the financial support from the National Natural Science Foundation of China (51933001, 52173174), the Natural Science Foundation of Shandong Province (no. ZR2022YQ45) and the Taishan Scholars Program (no. tstp20221121 and no. tsqnz20221134).

M.Z. acknowledge the funding supported by Postdoctoral Innovative Talent Support Program (Grant No. BX20220203) and China Postdoctoral Science Foundation (Grant No. 2022M722072). GIWAXS were performed at beamlines 7.3.3 and 11.0.1.2 at the Advanced LightSource, a U.S. DOE Office of Science User Facility under contract no. DE-AC02-05CH11231.

Author Contributions Statement

F.L., Z.B., L.Z. conceived and directed this project. R.Z. contributed to devices fabrication and characterization, and conducted the certification. M.Z. supported sample pretreatment, and W.Z., C.W., Z.F., T.R., carried out the GIWAXS and RSoXS measurement and assisted with data analysis. Xi.W., Y.L., H.L. and Z.B. supply NFREA materials. L.Z., Xu.W., H.J. carried out the TPV, TPC, impedance characterization and analyzed the data. B.H. supports rheological testing

and analysis.

G.Z. provided TAS results and corresponding analysis. J.D. and S.T. contribute to the ToF-SIMS and GPC measurements. J.Z. and Z.Z. conducted the AFM measurements. A.Z. contributed to sample preparation of cryo-TEM. F.H., J.X. contributed to the simulation results. X.X., S.X., and Y.Z. contributed to the fruitful discussion of this project. Y.L. supplied the calculation of FOM and relevant analysis. Y.L. contributed to *in-situ* absorption spectrum results. R.Z. wrote the manuscript,

M.Z. and F.L. contributed to revisions of the manuscript. This manuscript was mainly prepared by F.L., R.Z., M.Z., and all authors participated in the manuscript preparation and commented on the manuscript.

Competing Interests Statement

The authors declare no competing interests.

Table 1 | The efficiency for D18:2BTh-2F-C_2 BHJ in CF, OXY, CF&OXY condition under AM 1.5G, 100 mA cm^{-2}.

Solvent	J_{SC} (mA cm^{-2})	V_{OC} (V)	FF (%)	PCEa (%)	P_r (%)
CF	24.53 (24.08±0.56)	0.915 (0.917±0.002)	69.49 (67.81±2.60)	15.59 (14.97±0.43)	75.9
OXY	25.68 (25.71±0.39)	0.911 (0.912±0.001)	74.83 (72.52±1.48)	17.50 (17.00±0.27)	85.6
CF&OXY	26.71 (26.53±0.30)	0.913 (0.913±0.001)	77.98 (77.24±0.88)	19.02 (18.71±0.18)	92.3
certified	26.68	0.912	76.58	18.63	/

[a]The average values are obtained from 20 individual experimental results.

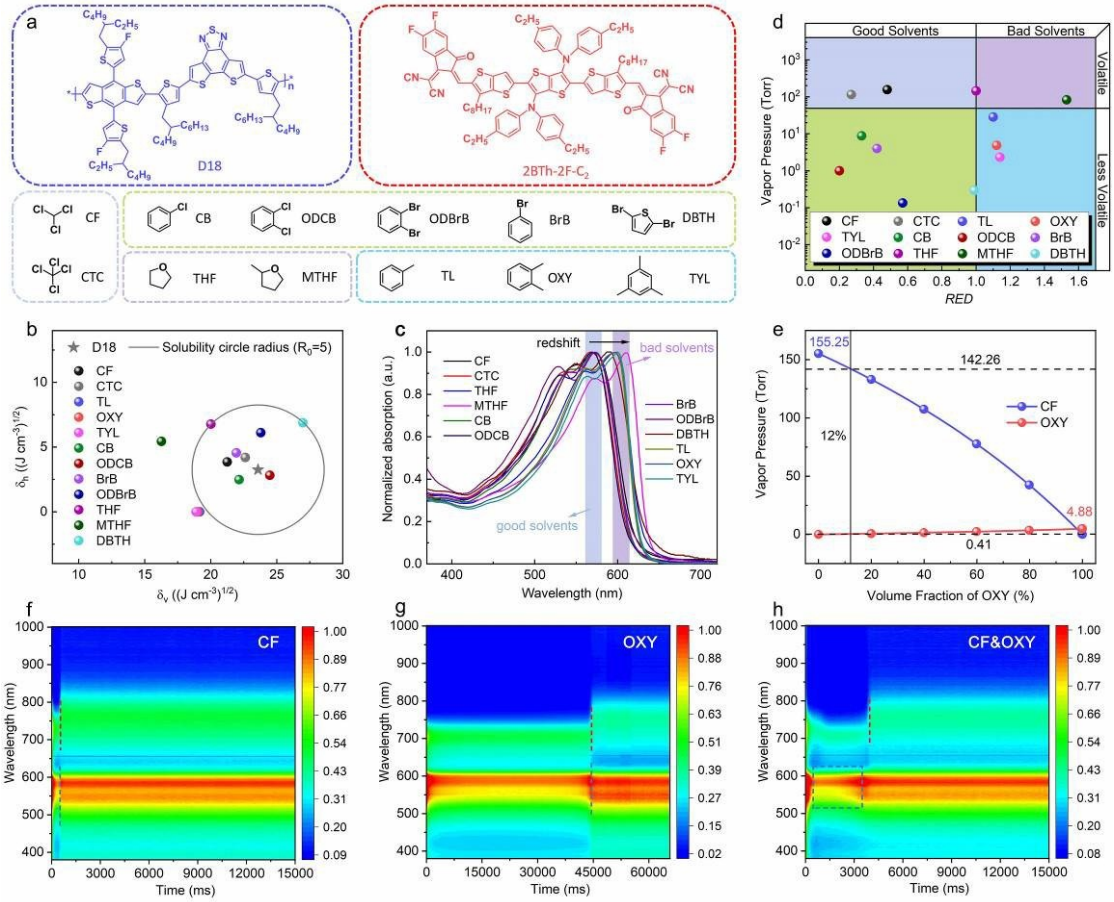

Fig. 1 | Materials and solvent selection. a, Chemical structures of D18, 2BTh-2F-C_2, and relevant solvents. **b,** Solubility of D18 in various solvents in the o_v–o_h diagram. (o_h: molecular hydrogen

bonding interactions; o_v: $\delta_t^2 = \delta_d^2 + \delta_p^2$) **c,** Normalized absorption of D18 in various solvents.

d, Solvent classification diagram based on vapor pressure and solubility. (*RED*: The relative energy difference) **e,** Vapor pressure as function of volume fraction in binary solvent of CF&OXY. Time- dependent contour maps of *in-situ* UV–vis absorption spectra for D18:2BTh-2F-C_2 blend precursor solutions in **f,** CF condition, **g,** OXY condition, **h,** CF&OXY condition.

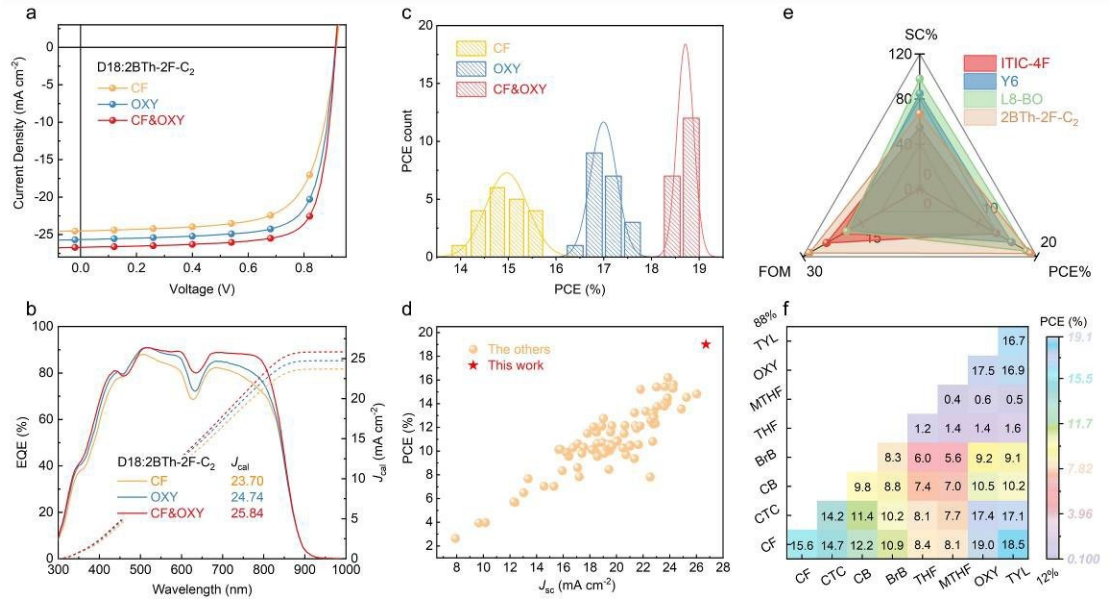

Fig. 2 | Devices performances. a, *J-V* curves and detailed parameters in different condition under AM 1.5G, 100 mA cm−2. **b,** EQE spectra and integrated J_{SC} in corresponding condition. **c,** Histogram of PCE measurement for devices in corresponding condition under AM 1.5G, 100 mA cm^{-2}. **d,** Plots of the PCE versus J_{SC} for the efficient NFREAs reported in the literature. Detailed data shown in Supplementary Table 9. **e,** Macroscopic factors matrix of SC, FOM and PCE based on IT-4F, Y6, L8-BO and 2BTh-2F-C_2. **f,** Efficiency for various solvent combinations under AM 1.5G, 100 mA cm^{-2}.

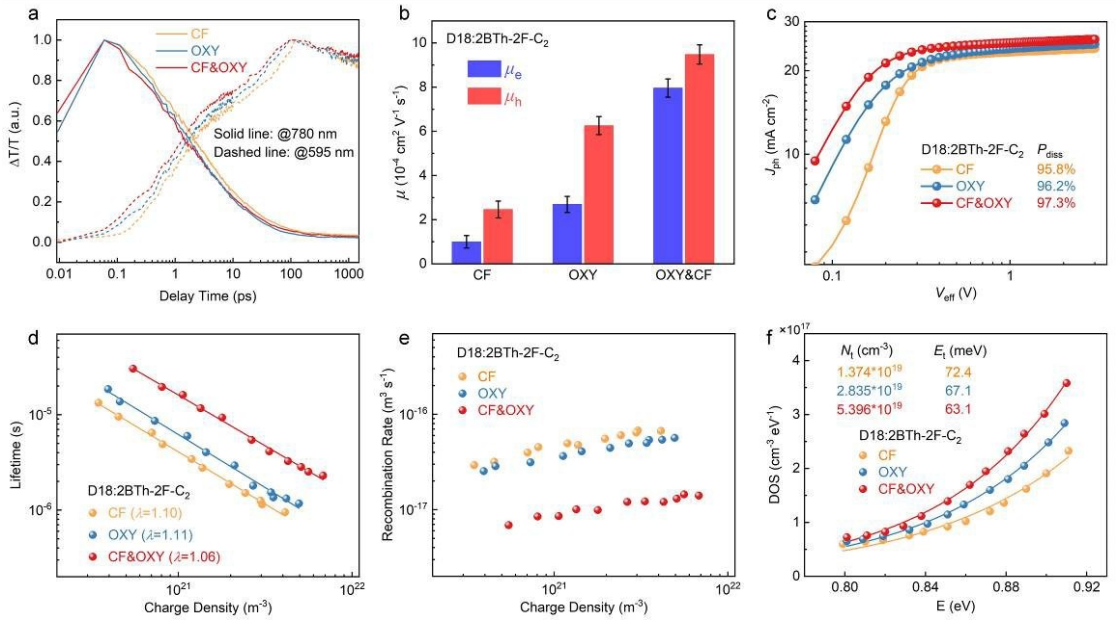

Fig. 3 | Ultrafast process and devices physical characteristics. a, Hole transfer process kinetics in corresponding conditions. **b,** Carrier mobility of the D18:2BTh-2F-C_2 in various conditions. (μ_e: the electron mobility; μ_h: the hole mobility) (The error bars represent the standard error) **c,** Photocurrent density (J_{ph}) versus effective bias (V_{eff}) characteristics in different conditions. (P_{diss}: carrier collection efficiency) **d,** Derived charge lifetime as a function of charge density fitted from TPV and TPC results, the exponential factor 11 is in relation to the non-geminate recombination order R (R=11+1, and R = 2 in ideal condition). **e,** Recombination rate coefficient as a function of charge density fitted from TPV and TPC results. **f,** Derived LUMO DOS from the capacitance spectra of devices and detailed parameters. (N_t: the total density per unit volume; E_t: the energy for exponential tail distribution that describes energetic disorder)

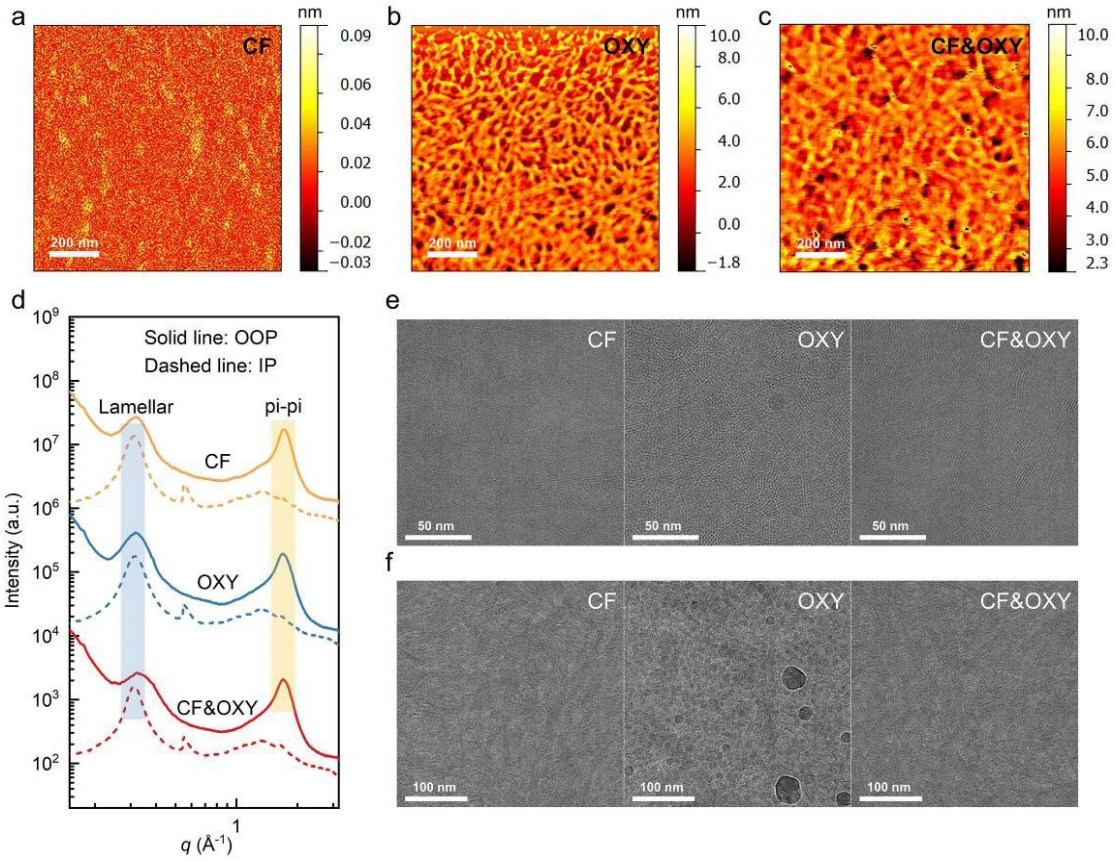

Fig. 4 | Morphology of thin films. Tapping AFM-IR topography image for D18:2BTh-2F-C_2 blends at the wavenumber of 1700 cm^{-1} in **a,** CF, **b,** OXY, **c,** CF&OXY condition. **d,** Line cut profiles for D18:2BTh-2F-C_2 blends in different conditions. Cryo-TEM images for CF, OXY, CF&OXY-based precursor solution in **e,** 50 nm scale and **f,** 100 nm scale.

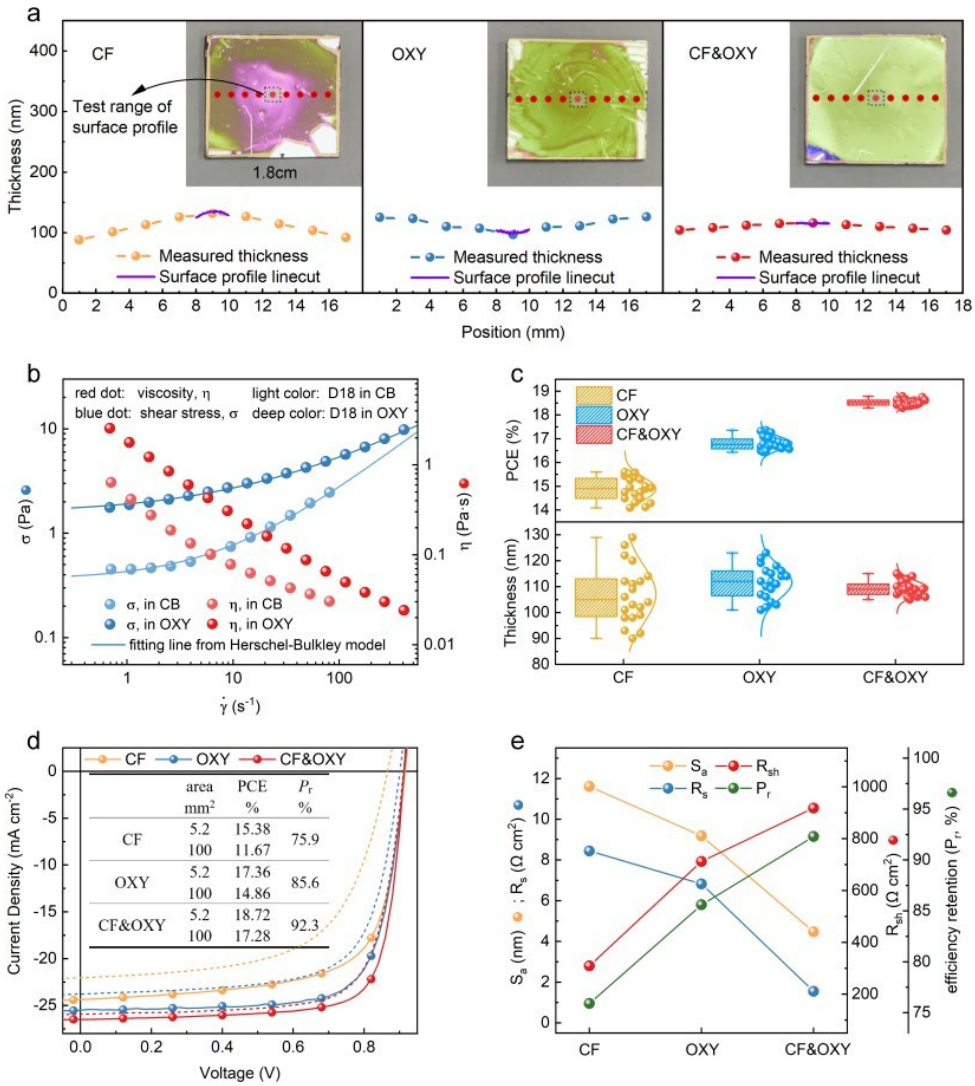

Fig. 5 | Rheological property and large-area devices. a, Measured thickness and surface profile linecut based on silicon wafer in CF, OXY, and CF&OXY condition, inset is the corresponding photograph. **b,** Rheological measurement for D18 in CB and OXY solution. **c,** Thickness and efficiency distribution of the devices in CF, OXY, and CF&OXY condition. (The error bars represent the upper and lower edges of the box plot) **d,** *J-V* curve and detailed parameters in CF, OXY, CF&OXY condition for 5.2 mm^2 (solid line) and 1 cm^2 (dash line) devices. **e,** Surface roughness (S_a), series resistance (R_s), shunt resistance (R_{sh}), and large-area device loss (P_r) for various conditions.